

Constraints on the gamma-ray emission from Small Solar System Bodies with the Fermi Large Area Telescope data

S. DE GAETANO ^{1,2} L. DI VENERE ¹ F. GARGANO ¹ F. LOPARCO ^{1,2} L. LORUSSO ^{1,2} M. N. MAZZIOTTA ¹
G. PANZARINI ^{1,2} R. PILLERA ^{1,2} AND D. SERINI ¹

¹*Istituto Nazionale di Fisica Nucleare, Sezione di Bari, via Orabona 4, I-70126 Bari, Italy*

²*Dipartimento di Fisica dell'Università e del Politecnico di Bari, via Amendola 173, I-70126 Bari, Italy*

ABSTRACT

All known Small Solar System Bodies have diameters between a few meters and a few thousands of kilometers. Based on the collisional evolution of Solar System Bodies, a larger number of asteroids with diameters down to ~ 2 m is thought to exist. As all Solar System Bodies, Small Bodies can be passive sources of high-energy gamma rays, produced by the interaction of energetic cosmic rays impinging on their surfaces. Since the majority of known asteroids are in orbits between Mars and Jupiter (in a region known as the Main Belt), we expect them to produce a diffuse emission close to the ecliptic plane. In this work we have studied the gamma-ray emission coming from the ecliptic using the data collected by the Large Area Telescope onboard the Fermi satellite. We have fit the results with simulations of the gamma-ray intensity at source level (calculated with the software FLUKA) to constrain the Small Solar System Bodies population. Finally, we have proposed a model describing the distribution of asteroid sizes and we have used the LAT data to constrain the gamma-ray emission expected from this model and, in turn, on the model itself.

1. INTRODUCTION

The Small Solar System Bodies (SSSBs) include asteroids, comets, small planetary satellites and all the other objects in the Solar System which are not planets, dwarf planets or natural satellites. These bodies can be mainly divided into three families: the Main Belt, including all small bodies lying between the orbits of Mars and Jupiter; the Trojans, which share an orbit with a larger planet or moon; and the Kuiper Belt, made of Trans-Neptunian objects. Asteroids are classified based on their color, albedo and spectral types (Lodders & Fegley 1998). About 75% of known asteroids belong to the C-type class. These asteroids are extremely dark, since their composition includes carbon in addition to rocks and minerals. The second most abundant taxonomic species are S-type asteroids, which represent 17% of the whole asteroids population. These asteroids are moderately bright and consist mainly of iron and magnesium silicates. Finally, most of the remaining

asteroids belong to the M-type class and are rich in metals (mainly iron and nickel).

All known asteroids have diameters > 2 m (assuming a spherical shape) and the majority is distributed along the ecliptic plane. As for all other objects in the Solar System, these bodies can be passive sources of gamma rays, produced by inelastic interactions of cosmic rays impinging on them. The result is the production of a diffuse gamma-ray emission along the ecliptic plane which, if observed, could provide a way to further investigate the asteroid properties and, in particular, to study the distribution of their sizes.

In the present work, we have studied the gamma-ray flux from the ecliptic plane using the data collected by the Fermi Large Area Telescope (LAT) from August 2008 to December 2020 and we have used these results to constrain the gamma-ray emission from SSSBs. In addition, we have used the FLUKA code to predict the gamma-ray emission resulting from CRs interacting with different types of asteroids. We have then used the analysis results to constrain the total number of asteroids with given properties. Finally, we have fit the LAT data with a diffuse flux model of the SSSBs, obtained by folding the gamma-ray intensity calculated with FLUKA with a population distribution function obtained by extending a model proposed by Davis et al.

Corresponding author: S. De Gaetano, L. Di Venere and M. N. Mazziotta
salvatore.degaetano@ba.infn.it, leonardo.divenere@ba.infn.it,
mazziotta@ba.infn.it

(2002) to diameters down to $\simeq 20$ cm. We have used the fit results to constrain the parameters of the diffuse flux and, in turn, the above-mentioned population model.

The idea of probing asteroid populations using gamma-ray observations was already considered by [Moskalenko et al. \(2008\)](#) and [Moskalenko & Porter \(2009\)](#), who also calculated the expected gamma-ray fluxes from asteroids under some simplifying assumptions. In the present work we propose a model that extends the previous ones, by including a description of the spatial morphology of the gamma-ray emission from asteroids.

2. SMALL SOLAR SYSTEM BODIES

The asteroid mass and size distributions are thought to result from collisions during their evolution and accretion. Collisions between asteroids give rise to a cascade of fragments, shifting masses toward smaller sizes, while slow accretion leads to the asteroid growth ([Dohnanyi 1969](#)). Under these assumptions, the size distribution can be described with a power-law model:

$$\frac{dN}{dr} = a r^{-\alpha} \quad (1)$$

where asteroids are modelled as spheres of radius r and the power-law index is $\alpha \simeq 2.7$.

Assuming that all the asteroids are homogeneous bodies with the same density ρ and a spherical shape, their mass distribution ($m = \frac{4\pi\rho}{3}r^3$) is also described by a power-law:

$$\frac{dN}{dm} = \frac{dN}{dr} \frac{dr}{dm} = \frac{a}{3} \left(\frac{4\pi\rho}{3} \right)^{\frac{\alpha-1}{3}} m^{-\frac{\alpha+2}{3}} = b m^{-\kappa} \quad (2)$$

with $\kappa = \frac{\alpha+2}{3}$ and $b = \frac{a}{3} \left(\frac{4\pi\rho}{3} \right)^{\frac{\alpha-1}{3}}$.

The parameter a can be calculated from the total mass M of the whole asteroid population. In fact, assuming that asteroid masses are distributed in the range from m_0 to m_1 , the total mass is given by:

$$M = \int_{m_0}^{m_1} m \frac{dN}{dm} dm = \begin{cases} b \frac{m_1^{2-\kappa} - m_0^{2-\kappa}}{2-\kappa} & \text{for } \kappa \neq 2 \\ b \log \frac{m_1}{m_0} & \text{for } \kappa = 2 \end{cases} \quad (3)$$

The parameter a is therefore given by:

$$a = \begin{cases} \frac{3M}{4\pi\rho} \times \frac{4-\alpha}{r_1^{4-\alpha} - r_0^{4-\alpha}} & \text{for } \alpha \neq 4 \\ \frac{3M}{4\pi\rho} \times \frac{1}{\log \frac{r_1}{r_0}} & \text{for } \alpha = 4 \end{cases} \quad (4)$$

where r_0 and r_1 are respectively the radii of asteroids with mass m_0 and m_1 .

The total mass of the asteroids in the Main Belt (semimajor axis $\simeq 2.7$ AU) and of Jovian Trojans (semimajor axis $\simeq 5.2$ AU) is estimated to be of about $10^{-4} - 10^{-3} M_{\oplus}$, where M_{\oplus} is the mass of the Earth, while the total mass of the asteroids in the Kuiper Belt beyond Neptune (semimajor axis $\simeq 40 - 50$ AU) is estimated to be about $10^{-2} M_{\oplus}$ ([Pitjeva & Pitjev 2018](#))¹.

The NASA Jet Propulsion Laboratory (JPL) database catalog ([Jet Propulsion Laboratory 2022](#)) provides the orbital parameters of almost 10^6 small bodies along with their diameters. The Trojan population is numerically 10–25% of the Main Belt population at sizes ≤ 100 km and the smallest diameter reported in the catalog is about 10^{-3} km. In [Fig. 1](#) the differential distribution of the radii of SSSBs found in the JPL database is shown. In [Davis et al. \(2002\)](#) several estimates of the Main Belt asteroid size distribution down to smaller diameters are presented.

The model in [Durda et al. \(1998\)](#) is a fit to the distribution determined by [Jedicke & Metcalfe \(1998\)](#), where the authors used the Spacewatch data to estimate the size distribution of SSSBs in the Main Belt. The estimate of the cumulative size distribution of asteroids (i.e., number of asteroids $N(d > D)$ with diameter d greater than a certain value D) is given and $N(d > 10^{-2} \text{ km}) \simeq 10^{10}$. In this work we extend the model down to diameters of $\simeq 20$ cm, extrapolating it with a log-parabola function. In particular, we assume the diameters to be distributed according to the JPL catalog for values above 2.5 km, and to follow the extrapolated model of [Durda et al. \(1998\)](#) for diameters in the range 20 cm – 2.5 km. The resulting model is shown in [Fig. 1](#) as a differential size distribution. In the same figure, we also show the distributions obtained assuming a power-law model as in [Eq. 1](#) for different values of the parameter α , with a total mass of the asteroids $M = 5 \times 10^{-4} M_{\oplus}$, $r_0 = 1 \times 10^{-4}$ km, $r_1 = 470$ km (Ceres' radius) and assuming an asteroid density

¹ The total asteroid mass is of the same order of magnitude as the mass of Moon, which is $\sim 10^{-2} M_{\oplus}$.

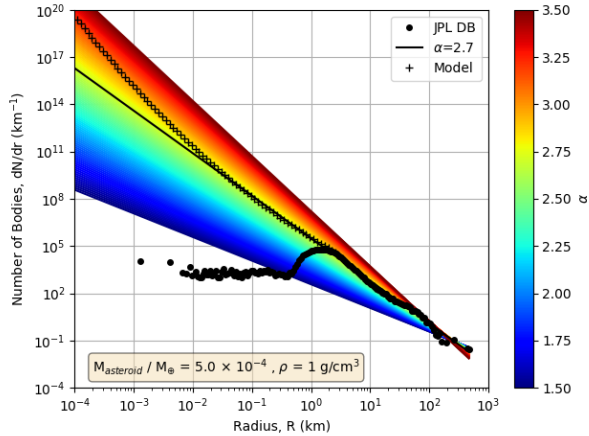


Figure 1. SSSBs size distribution. The distribution extracted from the JPL database is indicated with black circles, while the points of our model are indicated with black crosses. The colored bands show the power-law models (Eq. 1) for different values of α , assuming that the total mass of asteroids is $5 \times 10^{-4} M_{\oplus}$ and assuming an asteroid density of 1 g/cm^3 . The black line shows the differential size distribution with $\alpha = 2.7$.

of 1 g/cm^3 . In Fig. 1 the differential distribution of the radii of the bodies in the JPL catalog is also shown. The JPL catalog includes only observed objects; therefore the size distribution is underestimated for smaller radii as these objects are difficult to detect.

As explained in the following sections, the analysis of gamma rays detected by the LAT provides a way to set constraints on the population and size distribution of asteroids.

3. ASTEROIDS GAMMA-RAY EMISSION

As mentioned in the previous section, asteroids should produce a diffuse gamma-ray emission along the ecliptic plane due to interactions of charged cosmic rays with their surfaces. Hereafter we will assume the asteroids to be spherical. The gamma-ray flux produced by $N(r, d)$ asteroids of radius r at distance d from the Earth (in units of photons $\text{GeV}^{-1} \text{ cm}^{-2} \text{ s}^{-1}$) is given by the following equation (Ackermann et al. 2016; Mazziotta et al. 2020):

$$\phi_{\gamma}(E_{\gamma}, d, r) = \pi \frac{r^2}{d^2} I_{\gamma}(E_{\gamma}, r) N(r, d) \quad (5)$$

where E_{γ} is the gamma-ray energy and I_{γ} is the differential intensity of gamma rays at the production site.

3.1. Gamma-ray intensity at production

The gamma-ray intensity at production for an asteroid of radius r , in units of photons $\text{GeV}^{-1} \text{ cm}^{-2} \text{ sr}^{-1} \text{ s}^{-1}$, is given by:

$$I_{\gamma}(E_{\gamma}, r) = \sum_i \int Y_i(E_{\gamma}|E_k, r) I_i(E_k) dE_k \quad (6)$$

where $I_i(E_k)$ is the intensity of the i -th species of cosmic rays impinging on the asteroid surface (mostly protons, electrons and He nuclei) and $Y_i(E_{\gamma}|E_k, r)$ is the yield of gamma rays produced by the interaction of the i -th cosmic-ray species with kinetic energy E_k with the body surface of radius r .

We have calculated the yield $Y_i(E_{\gamma}|E_k, r)$ using the FLUKA code (Ferrari et al. 2005; Böhlen et al. 2014; Battistoni et al. 2015). FLUKA is a general purpose Monte Carlo code for the simulation of hadronic and electromagnetic interactions, used in many applications. It can simulate with high accuracy the interactions and propagation in matter of about 60 different species of particles, including photons and electrons from 1 keV to thousands of TeV, neutrinos, muons of any energy, hadrons and the corresponding antiparticles of energies up to 20 TeV or up to 10 PeV when it is interfaced with the DPMJET code (Roesler et al. 2001), neutrons down to thermal energies and heavy ions.

Hadronic interactions in FLUKA below a few GeV are based on resonance production and decay of particles, while for higher energies the Dual Parton Model is used, implying a treatment in terms of quark chain formation and hadronization. The interactions are simulated in the framework of the PreEquilibrium Approach to Nuclear Thermalization model (PEANUT) (Fassò et al. 2000; Battistoni et al. 2006), including the Gribov-Glauber multi-collision mechanism followed by the pre-equilibrium stage and eventually equilibrium processes (evaporation, fission, Fermi break-up and gamma deexcitation). We refer the reader to Mazziotta et al. (2016) and references therein for a more extended description on the interaction models that FLUKA employs for these interactions in different energy ranges. Full information on the different models used by the code and its related publications and references can be found in the FLUKA webpage².

The FLUKA code already has been used to model the gamma-ray emission from the Moon (Ackermann et al. 2016) and the Sun (Mazziotta et al. 2020), providing excellent agreement with data.

In our simulation setup, each SSSB is defined as a spherical body with radius ranging from 10 cm to

² <http://www.fluka.org/>.

100 km. We have simulated different kinds of bodies, with different compositions and densities.

We first defined three homogeneous bodies to investigate possible dependence on the simulated material and density:

- Ice: H₂O with density of 0.92 g cm⁻³
- Silica: SiO₂ with density of 2.00 g cm⁻³
- Carbon: C with density of 2.00 g cm⁻³

For ice, we assumed the same density as on the Earth. For silica and carbon bodies we chose the same density, in order to better investigate possible effects specifically due to the element.

Secondly, we defined two species which are representative of the most abundant asteroids:

- C-type asteroids, with a density of 2.23 g cm⁻³
- S-type asteroids, with a density of 3.80 g cm⁻³

We assumed that the C-type and S-type composition is the same as the one of carbonaceous and ordinary chondrites respectively, with the elemental abundances taken from tables 16.10 and 16.11 of (Lodders & Fegley 1998).

To evaluate the yields of secondary particles from the SSSBs we have simulated several samples of protons, electrons and ⁴He nuclei with different kinetic energies, impinging on the asteroids with an isotropic and uniform distribution. The primary kinetic energy values are taken on a grid of 81 equally spaced values in a logarithmic scale, from 100 MeV/n up to 10 TeV/n.

The differential yield of secondary particles produced by the i -th species of cosmic-ray primaries (here $i = p, e^-$ and ⁴He), $Y_i(E_\gamma|E_k, r)$, is calculated by counting the secondary particles which escape from the asteroid. The yield in units of GeV⁻¹ is defined as:

$$Y_i(E_\gamma|E_k, r) = \frac{N_i(E_\gamma|E_k, r)}{N_i(E_k)\Delta E_\gamma} \quad (7)$$

where $N_i(E_k)$ is the number of primaries of the i -th species generated with kinetic energy E_k (E_k is expressed in units of GeV for primary electrons and protons and of GeV/n for primary nuclei) and $N_i(E_\gamma|E_k, r)$ is the number of photons with energies between E_γ and $E_\gamma + \Delta E_\gamma$ produced by the primaries of the type i with kinetic energy E_k and escaping from the asteroid.

The intensities $I_i(E_k)$ at the asteroid position can be calculated starting from the local interstellar spectra (LIS) taking into account the propagation of CRs in

the Solar System, which is affected by solar activity. The activity of the Sun modulates the CR spectra with a 11-year cycle and its effect depends on the position of the asteroid in the Solar System. In this work we assume two limiting classes of CR spectra: the first one is given by the LIS, i.e. the spectra which are not affected by solar modulation, while the second are those measured at the Earth, where the solar modulation effect is larger than that at the positions of all asteroids, since their orbits are external to the Earth. In this way we are bracketing the asteroid emission between these two limiting cases, since asteroids are distributed at distances of 50 AU and beyond (see Fig. 7). We have taken the CR LIS from De La Torre Luque et al. (2021a,b, 2022). The CR spectra at the Earth have been precisely measured by the AMS-02 instrument. In particular, we have taken the proton spectrum from Aguilar et al. (2015a), the helium spectrum from Aguilar et al. (2015b, 2017) and the electron+positron spectrum from Aguilar et al. (2014). For the electron+positron spectrum at high energies we have also used the measurements by the Fermi-LAT (Abdollahi et al. 2017) and DAMPE (Ambrosi et al. 2017) (see also Mazziotta et al. 2020)³.

In addition, we expect a time-dependent gamma-ray signal due to the 11-year solar cycle, which modulates the cosmic-ray intensities. In particular, this modulation is observed in the Moon gamma-ray flux, with variations over one Solar cycle in the range $\pm 15\%$ of the average emission (Ackermann et al. 2016; De Gaetano et al. 2021).

Fig. 2 shows the gamma-ray intensities (Eq. 6) evaluated for the different classes of asteroids simulated in this work⁴. Most lines in the spectra are due to photons emitted in nuclear de-excitation processes. The line at 511 keV is due to annihilations of positrons produced in the electromagnetic showers. The line at 2.2 MeV, which is visible in the ice bodies, is due to neutron capture by hydrogen nuclei, with the production of a deuterium nucleus and the emission of a gamma ray. Other classes of asteroids exhibit characteristic lines related to their composition. We remark that these features can be of particular interest for in-situ studies of asteroid composition. The gamma-ray intensities from the different classes of asteroids are also compared with

³ We did not simulate electrons and positrons separately, but only primary electrons assuming a spectrum equal to the overall electron+positron one.

⁴ As an example, in appendix A we report detailed plots of gamma-ray yields and intensities for the different particle species interacting with Silica asteroids.

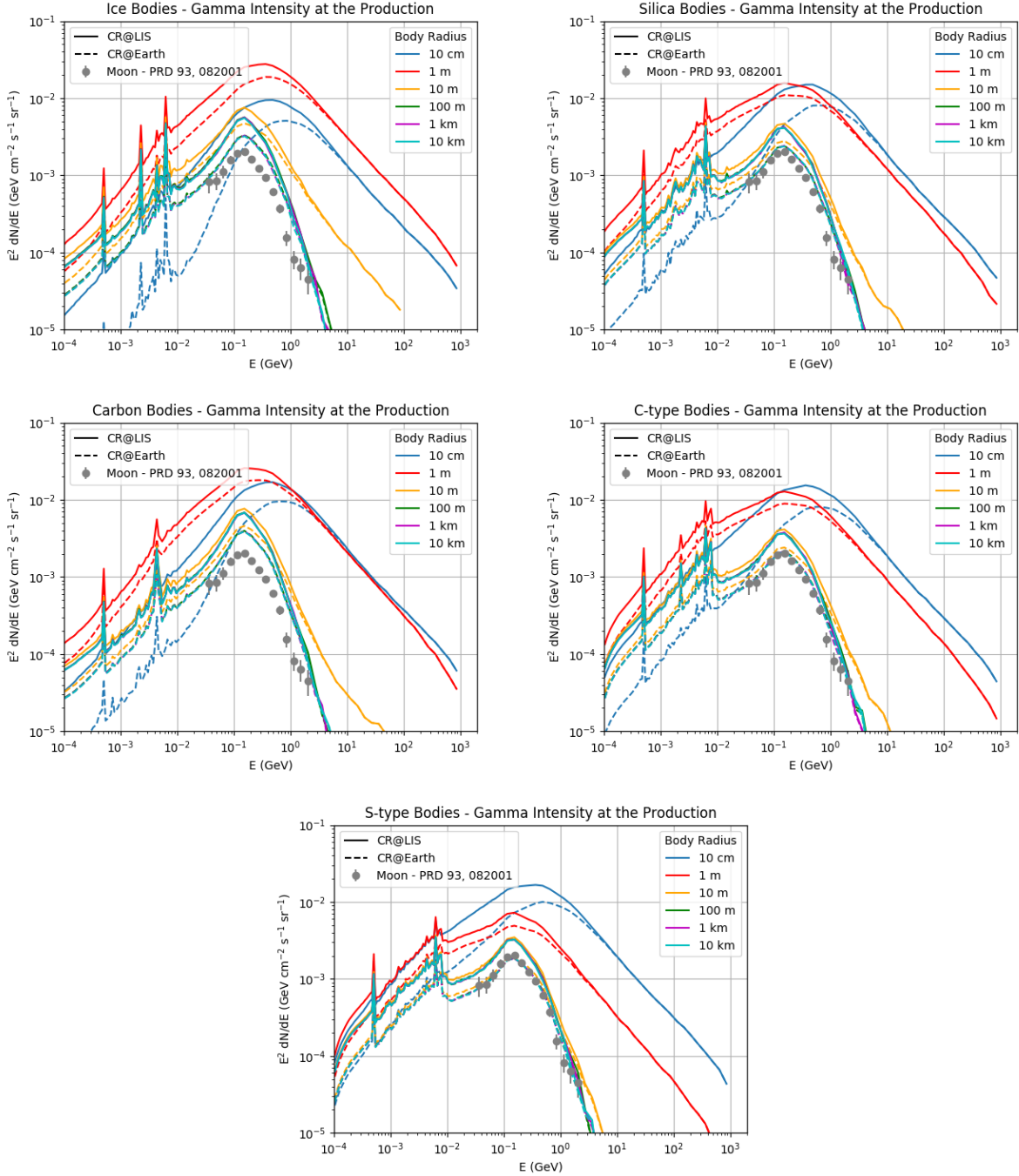


Figure 2. Gamma-ray intensities (multiplied by the energy squared) from ice, silica, carbon, C-type and S-type asteroids. The spectra have been evaluated assuming different radii, from 10 cm to 10 km. The calculations have been performed in the two limiting cases, using the CR LIS spectra (continuous lines) and the CR spectra measured at Earth (dashed lines). The gray points show the intensity of the Moon measured by the Fermi-LAT (Ackermann et al. 2016).

the gamma-ray intensity from the Moon measured by the Fermi LAT (Ackermann et al. 2016). We see that the intensity of gamma rays emitted from silica bodies of large sizes is close to the intensity of gamma rays emitted from the Moon.

Fig. 3 shows the integral of the intensity above 0.1 GeV as a function of the asteroid radius for the different classes of asteroids. It can be noticed that the intensity at the production site drops for radii smaller than 1 m, since the asteroid size becomes comparable or smaller than the typical interaction length in the

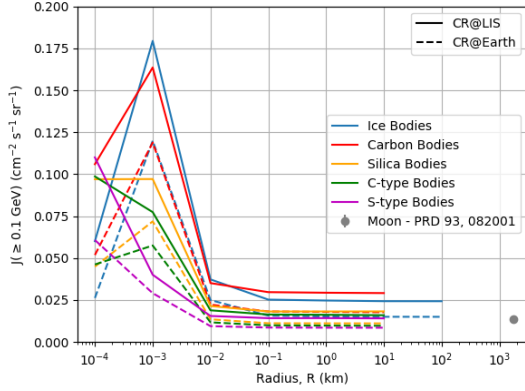


Figure 3. Gamma-ray intensity above 0.1 GeV as a function of the body radius using the CR LIS spectra (continuous lines) and the CR spectra measured at Earth (dashed lines). The colored lines indicate the different compositions. The gray point shows the Moon data measured by the Fermi-LAT (Ackermann et al. 2016).

simulated materials, which are of the order of tens of centimeters. From Figs. 2 and 3 we see that for $r > 10$ m the shapes of the spectra (and consequently the integral of the intensity above 0.1 GeV) do not depend on the asteroid radius and are similar to the shape of the gamma-ray intensity from the Moon (Ackermann et al. 2016). This is because the secondary gamma rays produced by cosmic rays impinging on the asteroids can escape only from external layers, since the cosmic-ray nuclei can penetrate down to depths of a few tens of grams per centimeter squared (corresponding to the hadronic interaction length for protons and He nuclei), while the gamma-ray absorption length (corresponding to the radiation length) is shorter. When the asteroid size is larger than both of these characteristic lengths, the gamma-ray production becomes independent of the size.

3.2. Gamma-ray flux at the Earth

Fig. 4 shows the gamma-ray fluxes at the Earth from asteroids of different classes and different radii at a distance of 2.7 AU from our planet, evaluated using Eq. 5 with $N(r, d) = 1$.

The gamma-ray flux produced by asteroids of radius $r > r_0$ (cumulative flux) at a given distance d is given by:

$$\phi_\gamma(E_\gamma, d, r > r_0) = \int_{r_0}^{r_1} \frac{\pi r^2}{d^2} I_\gamma(E_\gamma, r) \frac{dN}{dr} dr, \quad (8)$$

where $r_1 \sim 500$ km is the largest radius of observed asteroids.

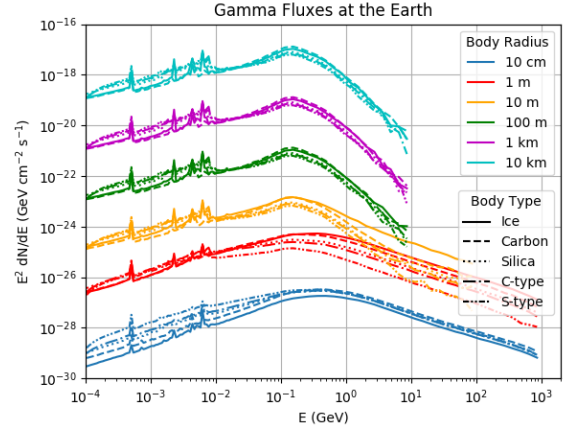


Figure 4. Gamma-ray fluxes at the Earth (multiplied by the energy squared) from single spherical bodies of different radii and types at the distance of 2.7 AU from the Earth.

Fig. 5 shows the cumulative gamma-ray fluxes at the Earth calculated with a population of SSSBs shown in Fig. 1 at a distance of 2.7 AU, for different values of r_0 in the range from 10 cm to 10^3 km.

As discussed above, the gamma-ray emission at the site of production is almost independent of size for asteroid radii larger than a few tens of meters. Assuming that the gamma-ray intensity I_γ does not depend on the asteroid radius r , the gamma-ray flux at the Earth for a power-law size distribution of the asteroids at a given distance d can be expressed as:

$$\begin{aligned} \phi_\gamma &= \pi I_\gamma \int_{r_0}^{r_1} \frac{r^2}{d^2} a r^{-\alpha} dr = \\ &= \begin{cases} \pi I_\gamma \frac{a}{d^2} \frac{r_1^{3-\alpha} - r_0^{3-\alpha}}{3-\alpha} & \text{for } \alpha \neq 3 \\ \pi I_\gamma \frac{a}{d^2} \log \frac{r_1}{r_0} & \text{for } \alpha = 3 \end{cases} \quad (9) \end{aligned}$$

where r_0 and r_1 are the minimum and maximum asteroid radii and the parameter a can be calculated from Eq. 4.

Following Ackermann et al. (2016), the gamma-ray flux from the Moon can be expressed as:

$$\phi_\zeta = \pi I_\gamma \frac{R_\zeta^2}{D_\zeta^2} \quad (10)$$

where I_γ is the intensity of lunar gamma rays, while R_ζ and D_ζ indicate the lunar radius and the Earth-Moon distance, respectively.

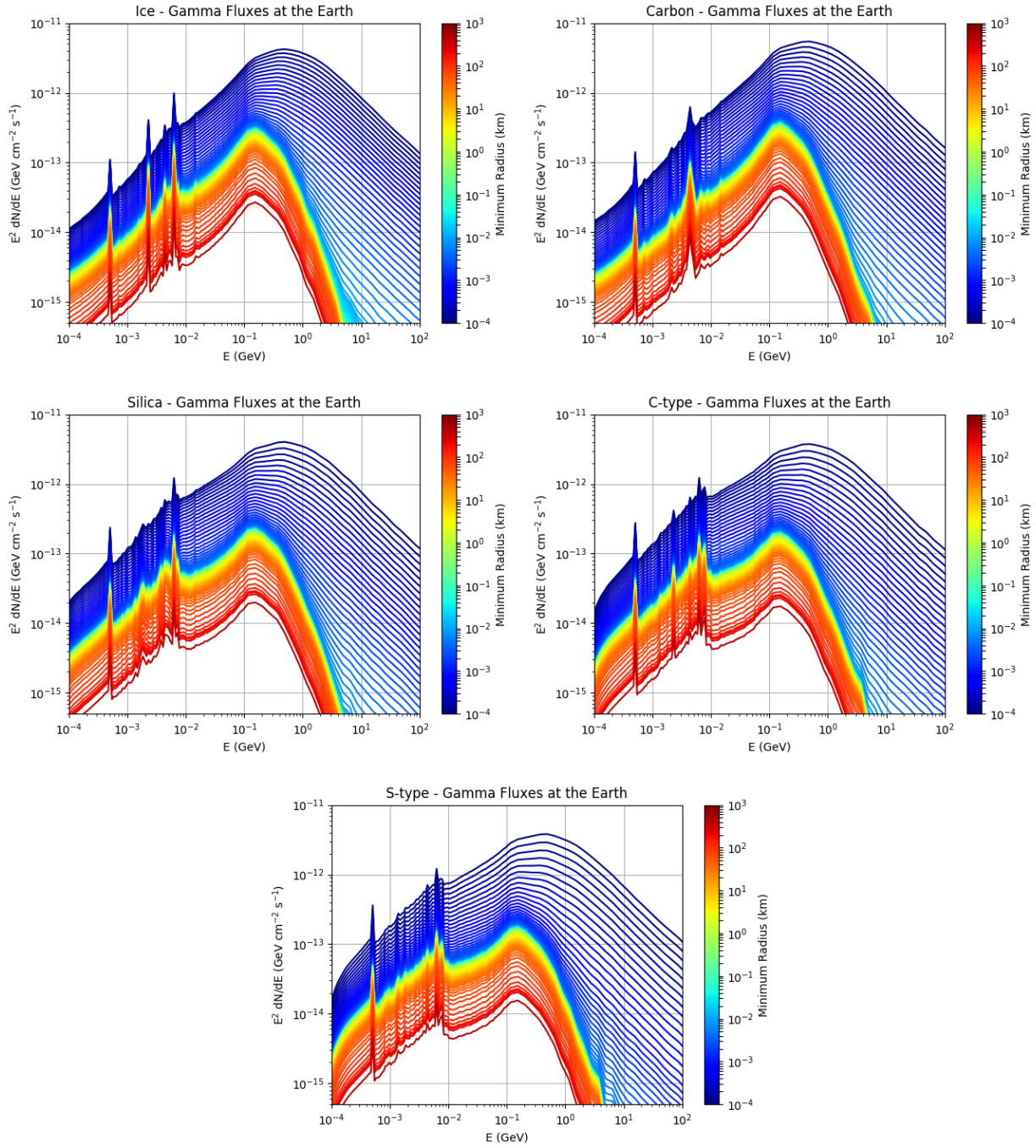


Figure 5. Cumulative gamma-ray fluxes (multiplied by E_γ^2) at the Earth for the SSSB population model described in section 2 and shown in Fig. 1. Top-left panel: ice bodies; top-right panel: carbon bodies; middle-left panel: silica bodies; middle-right panel: C-type bodies; bottom panel: S-type bodies. The colored lines correspond to different values of the minimum asteroid radius \bar{r} .

From the results shown in Figs. 2 and 3, assuming that the gamma-ray intensity from asteroids is the same as from the Moon ⁵, from eqs. 9 and 10 it follows that:

$$\frac{\phi}{\phi_{\zeta}} = \begin{cases} a \frac{1}{R_{\zeta}^2} \frac{D_{\zeta}^2}{d^2} \times \frac{r_1^{3-\alpha} - r_0^{3-\alpha}}{3-\alpha} & \text{for } \alpha \neq 3 \\ a \frac{1}{R_{\zeta}^2} \frac{D_{\zeta}^2}{d^2} \times \log \frac{r_1}{r_0} & \text{for } \alpha = 3 \end{cases} \quad (11)$$

We remark that Eq. 11 differs from Eq. 6 in Moskalenko et al. (2008), where it was assumed that the emission from small bodies scales with the radius of the body. In this work we calculate the gamma-ray flux from each body as in Eq. 5. For radii larger than ~ 10 m, the intensity at production becomes independent of the radius, as discussed above, and the flux at the Earth scales with the square of the radius. As a consequence, assuming a population of asteroids with radii between $r_0 = 1 \times 10^{-4}$ km and $r_1 = 470$ km, following Eq. 11 our model predicts an asteroid flux from two to six orders of magnitudes lower than the flux calculated in Eq. 6 in Moskalenko et al. (2008), depending on the index α of the power-law describing the asteroid size distribution.

3.3. Spatial map of small bodies

Since the orbits of the asteroids lie in an extended region of the sky, to build a template describing their gamma-ray emission we have first divided the sky into equal solid angle pixels and then we have added together the contributions from individual pixels.

The differential gamma-ray flux from the SSSBs of radius r in a sky pixel at the ecliptic coordinates (λ, β) , covering a solid angle $\Delta\Omega$ is given by:

$$\phi_{\gamma}(E_{\gamma}, r, \lambda, \beta) = \sum_{i \in \text{l.o.s.}} \frac{N(\lambda, \beta, r, d_i)}{\Delta\Omega} \frac{\pi r^2}{d_i^2} I_{\gamma}(E_{\gamma}, r) \quad (12)$$

where the summation is extended to all the bodies lying along the line-of-sight (l.o.s.) in the direction (λ, β) . In Eq. 12 we have indicated with $N(\lambda, \beta, r, d_i)$ the number of asteroids along the line-of-sight at distance d_i from the Earth, with radius r .

⁵ We note that the CR intensities are not the same at the asteroid and Moon positions, and therefore the gamma-ray intensities are slightly different (see discussion in Sect. 3).

We can then define the fraction of bodies at distance d_i within the cone pointing towards the direction (λ, β) as:

$$w(\lambda, \beta, r, d_i) = \frac{N(\lambda, \beta, r, d_i)}{N_{tot}(r)} \quad (13)$$

where $N_{tot}(r)$ is the total number of bodies of radius r in the sky. With this definition, Eq. 12 can be rewritten as follows:

$$\phi_{\gamma}(E_{\gamma}, r, \lambda, \beta) = \frac{1}{\Delta\Omega} \sum_{i \in \text{l.o.s.}} w(\lambda, \beta, r, d_i) \frac{\pi r^2}{d_i^2} I_{\gamma}(E_{\gamma}, r) N_{tot}(r). \quad (14)$$

If we assume that all SSSBs are equally distributed in the sky, w is independent of r . Therefore, Eq. 14 can be rewritten as:

$$\phi_{\gamma}(E_{\gamma}, r, \lambda, \beta) = \pi r^2 I_{\gamma}(E_{\gamma}, r) N_{tot}(r) \sum_{i \in \text{l.o.s.}} \frac{w(\lambda, \beta, d_i)}{\Delta\Omega d_i^2} \quad (15)$$

The r.h.s. of Eq. 15 can then be viewed as the product of two factors: a spectral factor, given by the intensity at production for an asteroid of radius r , weighted by a factor πr^2 and by the number of asteroids with radius r ; and a spatial factor, containing the fraction of bodies at given spatial coordinates, divided by the solid angle $\Delta\Omega$, weighted with the inverse of their squared distance from the Earth and summed along l.o.s. If the spatial factor and $I_{\gamma}(E_{\gamma}, r)$ are known or estimated, by fitting the LAT data with the model in Eq. 15, it is possible to set constraints on the distribution $N_{tot}(r)$. To build a spatial map of the asteroid emission, we start by estimating the spatial factors for different directions (λ, β) . An asteroid orbit is characterized by four parameters:

- the orbit major semiaxis l ;
- the inclination angle i of the orbit with respect to the ecliptic plane;
- the longitude Ω of the ascending node (i.e. one of the two intersection points between the asteroid orbit and the ecliptic plane), measured with respect to the direction of the First Point of Aries;
- the argument of periapsis ω , i.e. the angle between the ascending node direction and the major semiaxis.

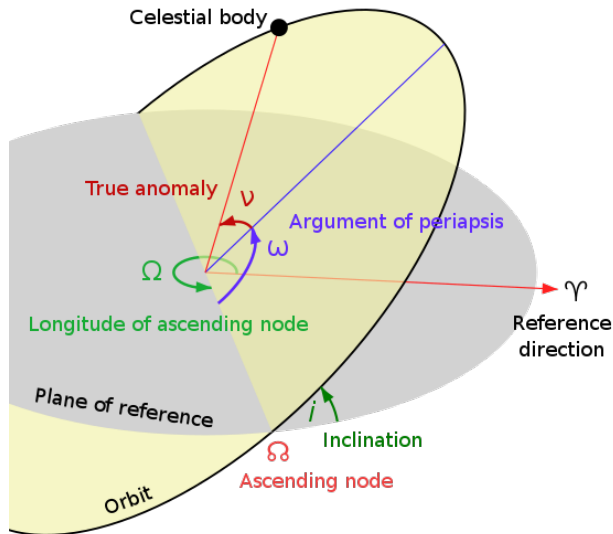


Figure 6. Graphical representation of the orbit of an asteroid (Wikipedia 2022).

The asteroid position on its orbit is identified by the angle ν that its direction forms with respect to the major semiaxis, called “true-anomaly” angle. A graphical representation of an asteroid orbit is shown in Figure 6.

Fig. 7 shows the distributions of the orbital parameters of the SSSBs found in the JPL catalog. We verified that such parameters are not correlated with each other. To build a spatial map of the asteroid population, we sampled 10^7 times the orbital parameters, assuming circular orbits, and extracting the true-anomaly angles from a uniform distribution between 0° and 360° . For each set of parameters l , i , Ω , ω and ν , the corresponding asteroid position can be evaluated in a right-handed reference frame centered on the Sun with the x -axis directed from the Sun to the First Point of Aries, and the z -axis perpendicular to the ecliptic plane. In this frame, the position of the asteroid is given by:

$$\begin{aligned} x_A &= l[\cos \Omega \cos(\omega + \nu) - \sin \Omega \cos i \sin(\omega + \nu)] \\ y_A &= l[\sin \Omega \cos(\omega + \nu) - \cos \Omega \cos i \sin(\omega + \nu)] \\ z_A &= l \sin i \sin(\omega + \nu) \end{aligned} \quad (16)$$

From Eq. 16 the ecliptic coordinates of the asteroid can be evaluated:

$$\begin{aligned} \lambda_{ecl} &= \arctan \frac{y_A}{x_A} \\ \beta_{ecl} &= \arcsin \frac{z_A}{\sqrt{x_A^2 + y_A^2 + z_A^2}} \end{aligned} \quad (17)$$

By following the prescriptions in Duffett-Smith & Zwart (2011), the ecliptic coordinates of each body can be converted into celestial and galactic coordinates.

If the Sun-Earth direction forms an angle ξ with respect to the x -axis, the Earth coordinates (in AU units) are given by $x_E = \cos \xi$, $y_E = \sin \xi$, $z_E = 0$. For each simulated asteroid position we extracted the angle ξ describing the position of the Earth from a uniform distribution between 0° and 360° . The asteroid distance from the Earth is therefore given by $d = \sqrt{(x_A - x_E)^2 + (y_A - y_E)^2 + (z_A - z_E)^2}$.

The asteroid spatial map is built using a HEALPix⁶ pixelization of the sky with $N_{side} = 32$. This means that the sky is divided into $12 \times N_{side}^2 = 12288$ pixels, each one with solid angle $\Delta\Omega = 1.02 \times 10^{-3}$ sr. Each pixel is assigned a weight given by the spatial factor in Eq. 15:

$$\bar{w}(\lambda, \beta) = \frac{1}{\Delta\Omega} \sum_{i \in l.o.s.} \frac{w(\lambda, \beta, d_i)}{d_i^2} \quad (18)$$

where λ and β are the coordinates at the center of the given pixel, $N(\lambda, \beta, d_i)$ is the number of objects with distance d_i from the Earth whose coordinates are contained in that pixel and N is the total number of simulated asteroids.

The asteroid spatial maps are shown in Fig. 8. The top panel shows the asteroid distribution in ecliptic coordinates. The middle panel shows the average asteroid distance from the Earth as a function of the asteroid position. We see that the asteroid distribution is peaked toward the direction of the Sun (which is at the center of the map). This projection effect results from the asteroids along the Earth-Sun direction being, on average, farther from the Earth than those along the opposite direction. Finally, the bottom panel shows the spatial template of Eq. 18 in celestial coordinates.

4. LAT DATA ANALYSIS

The LAT is a gamma-ray pair conversion telescope, designed to detect photons in the energy range from 20 MeV up to more than 300 GeV. It consists of a 4×4 array of 16 identical towers, each one composed of a tracker (TKR) and a calorimeter (CAL) module. Incident gamma rays are converted into e^+e^- pairs, whose energies and directions are measured by the CAL and the TKR, thus providing information on the photon energy and direction. The TKR contains 36 alternating layers of silicon strip detectors interleaved with tungsten converter foils, for a total on-axis thickness of 1.5 radiation lengths. The CAL consists of 96 CsI (TI) crystals, hodoscopically arranged in 8 layers, for a total on-axis thickness of 8.6 radiation lengths. The towers are surrounded by a segmented anticoincidence

⁶ <http://healpix.sourceforge.net>

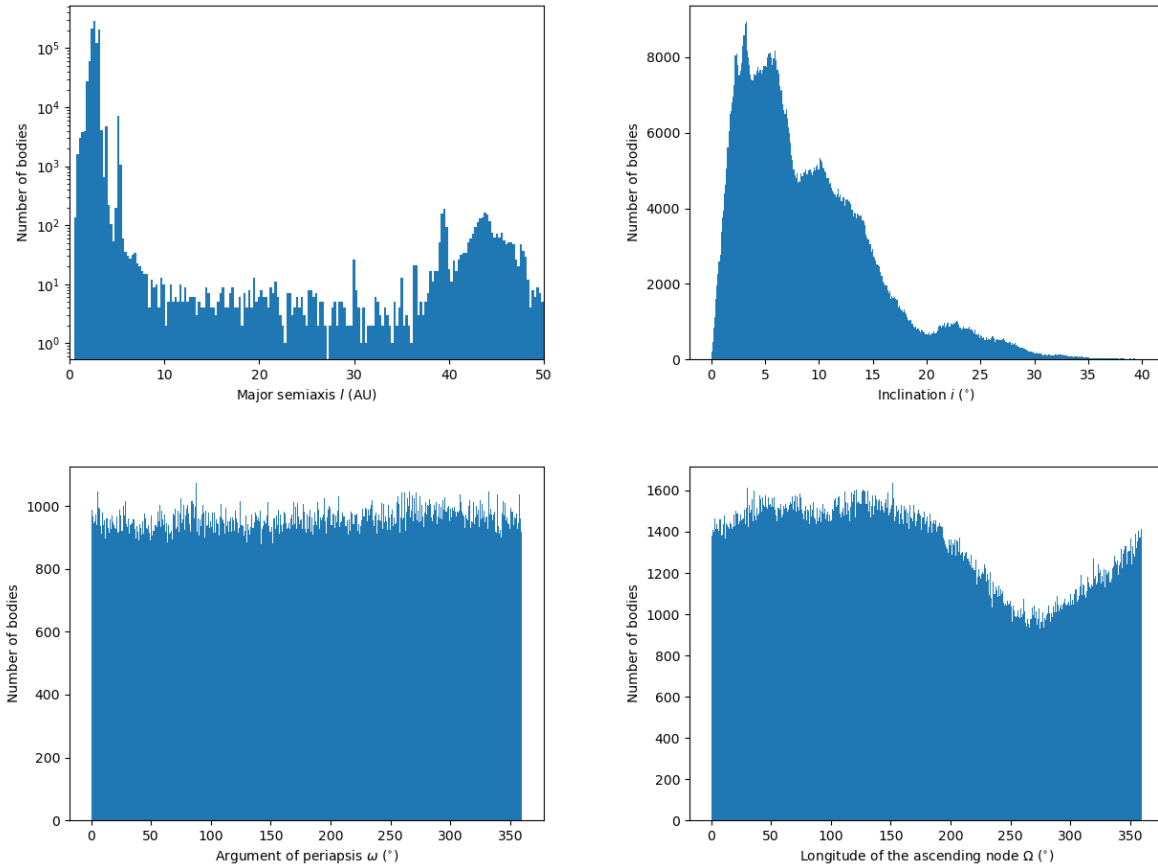


Figure 7. Distributions of the orbital parameters of the SSSBs in the JPL catalog. Top left: major semiaxis; top right: inclination; bottom left: argument of periapsis; bottom right: ascending node longitude.

detector (ACD), made of plastic scintillators, working as a veto for charged cosmic rays. Detailed descriptions of the instrument can be found in [Atwood et al. \(2009\)](#) and [Abdo et al. \(2009\)](#); [Ackermann et al. \(2012\)](#).

The data sample used for the present analysis has been extracted from the *Pass 8 P305* dataset ([Atwood et al. 2013](#)), selecting ULTRACLEANVETO event class (front and back) photons ⁷, with energies between 56 MeV and 1.78 TeV, collected in the period from August 2008 (MET=239557418) to December 2020 (MET=631153850) ⁸. The energy interval has been divided into logarithmic bins, with 8 bins per decade. The analysis has been performed in six different Regions

of Interest (RoIs) along the ecliptic plane, of 40° width in equatorial latitude and longitude, thus selecting the parts of the sky where the asteroid signal is expected to be maximal. A minimum separation of $\simeq 17^\circ$ from the Galactic Equator was required, in order to avoid the strong contamination from the diffuse interstellar gamma-ray emission in the Milky Way. The resulting RoIs are centered at the ecliptic longitudes 0° , 40° , 140° , 180° , 220° and 320° , and at the ecliptic latitude 0° (see [Fig. 9](#)). In the following we will designate these regions as RoI 0, RoI 40, RoI 140, RoI 180, RoI 220 and RoI 320.

We selected the time intervals when the LAT was operating in its standard science operation configuration and was outside the South Atlantic Anomaly (SAA). To limit contamination from the Earth limb, we discarded time intervals when the LAT z-axis was at an angle $> 70^\circ$ with respect to the zenith direction. This tight zenith cut has been implemented to take into account the broad instrument point spread function (PSF) below 100 MeV. When selecting the good time intervals for the data analysis, we also required a minimum

⁷ This is the event class with the smallest fraction of residuals (misclassified) cosmic rays and is recommended for studies of diffuse emission (see <https://fermi.gsfc.nasa.gov>).

⁸ The Mission Elapsed Time, or MET, is the number of seconds since the reference time of January 1, 2001, at 0h:0m:0s in the Coordinated Universal Time (UTC) system, corresponding to a Modified Julian Date (MJD) of 51910 in the UTC system (see https://fermi.gsfc.nasa.gov/ssc/data/analysis/documentation/Cicerone/Cicerone_Data/Time_in_ScienceTools.html).

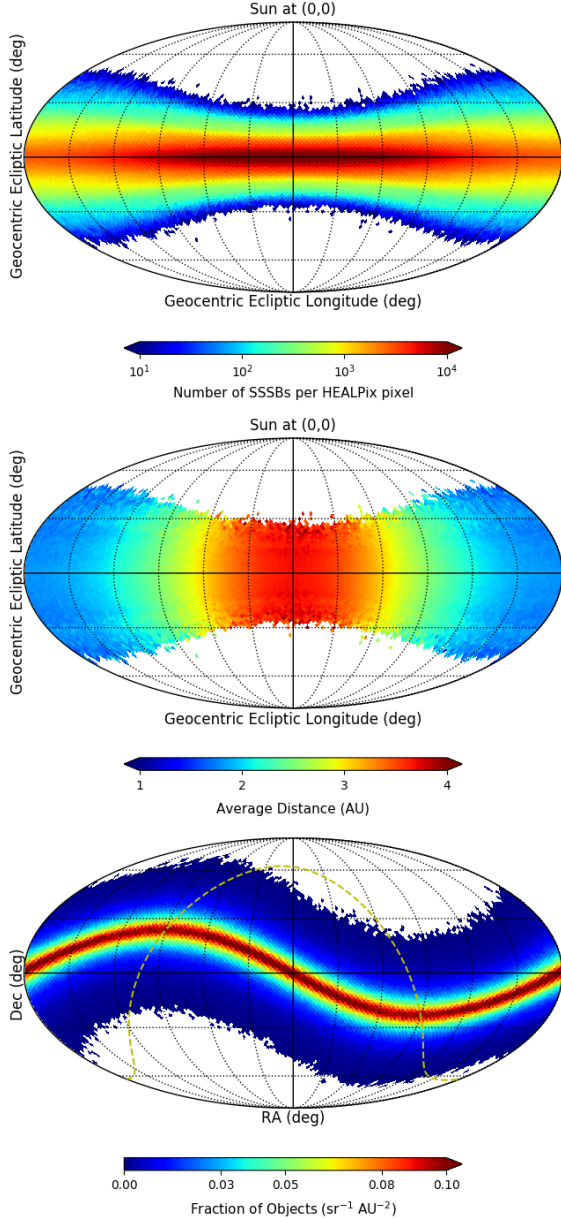


Figure 8. Spatial maps of asteroids obtained from the simulation. Top panel: number of SSSBs per HEALPix pixel in ecliptic coordinates. Middle panel: average asteroid distance from the Earth as a function of its position in the sky. Bottom panel: spatial template of the asteroids (Eq. 18) in equatorial coordinates, built using a HEALPix pixelization of the sky with $N_{side} = 32$ (Mollweide projection). The dashed yellow line represents the galactic plane.

angular separation of 35° (45°) between the Moon (Sun) direction and the center of each RoI, to avoid

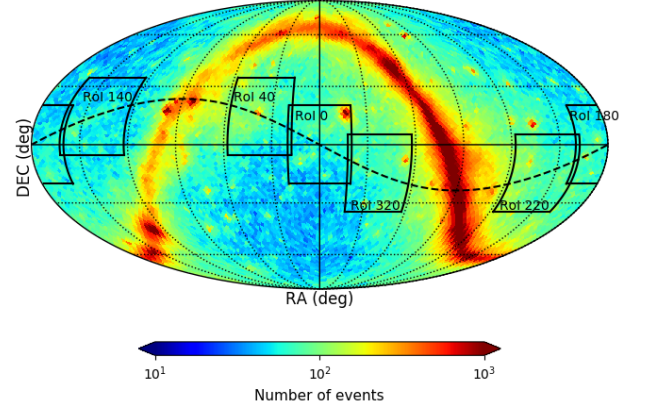


Figure 9. Spatial map in J2000 right ascension and declination of all events detected by the LAT in August 2008 with energy between 56 MeV and 1 TeV and zenith angle $> 90^\circ$ (Mollweide projection). The boundaries of the six analysis RoIs are also indicated by the black continuous lines.

contamination from lunar (solar) gamma rays⁹. Due to the cut on the angular separation from the Sun, each RoI is excluded from coverage for a few months of the year.

The analysis was performed using the `fermitools` (version 2.0.8)¹⁰ and `fermipy` (version 1.0.1) (Wood et al. 2018) packages. For each of the six RoIs, the analysis was performed separately in each month of each year of the selected data sample. In fact, a possible diffuse signal from the asteroids should be time-dependent, since the relative motion of Earth and asteroids implies variations of the spatial map template of Eq. 18, due to changes in the relative distances and in the subtended solid angles. In addition, solar modulation could yield variations observable on yearly/monthly timescales (Ackermann et al. 2016; De Gaetano et al. 2021).

We have implemented a fitting procedure based on a Poisson maximum likelihood approach. The gamma-ray emission from each RoI is modeled including the standard diffuse background templates developed by the Fermi-LAT collaboration, i.e. the Galactic Interstellar Emission model `gll_iem_v07.fits` and the isotropic model¹¹. The point-like and extended sources in each RoI are taken from the fourth catalog of LAT sources 4FGL (Abdollahi et al. 2020). The normalization parameters of the diffuse models and of all the sources

⁹ We did not implement any cut on the positions of major planets since the LAT has not yet detected emission from any of them.

¹⁰ <https://fermi.gsfc.nasa.gov/ssc/data/analysis/software/>

¹¹ <https://fermi.gsfc.nasa.gov/ssc/data/access/lat/BackgroundModels.html>

within 25° from the center of the RoI and detected with $\text{TS} > 25$ were fitted. An additional source was added to describe the asteroid emission, as discussed in Section 3. As previously explained, we used the map in Eq. 18 and shown in Figure 8 as a spatial template. To minimize the assumptions on the spectral shape, a power-law with spectral index 2 was used¹²:

$$\frac{dN_\gamma}{dE} = N_{0,\gamma} \left(\frac{E}{E_0} \right)^{-2} \quad (19)$$

with $E_0 = 100$ MeV. Here $N_{0,\gamma}$ is the differential flux at $E = E_0$, in units of $\text{MeV}^{-1}\text{cm}^{-2}\text{s}^{-1}$ and is the only free parameter in this model.

For each fit, we computed the Test Statistic (TS) for the spatial template representing the diffuse emission due to asteroids, defined as

$$\text{TS} = -2(\ln \mathcal{L}_{max,0} - \ln \mathcal{L}_{max,1}) \quad (20)$$

where $\mathcal{L}_{max,0}$ is the maximum likelihood value for a model without the source of interest (the ‘‘null hypothesis’’) and $\mathcal{L}_{max,1}$ is the maximum likelihood value for a model with the additional source (‘‘alternative hypothesis’’), which, in this case, is represented by the asteroids. The TS is usually used to estimate the significance of the source. In particular, in the case of a model with one additional degree of freedom with respect to the null hypothesis, the significance is equal to $\sqrt{\text{TS}}$.

Figure 10 shows a summary of the fit results obtained in the analysis of the different RoIs in the different time intervals. The top panels of Figure 10 show the values of the normalization constants of the Galactic interstellar and of the isotropic diffuse components obtained from the fits. In all fits the TS turned out to be $\simeq 0$, i.e. the asteroid source was not significantly detected for any RoI and time interval. Hence, in each fit we derived the upper limit (UL) on the asteroid flux above 56 MeV at 95% confidence level (CL). These limits are shown in the bottom panels of Figure 10. We see that the distributions of the ULs on the asteroid flux obtained in the various RoIs exhibit similar shapes and are peaked around $2 \times 10^{-5} \text{ MeV}^{-1}\text{cm}^{-2}\text{s}^{-1}$. The normalization constants are close to 1, with the normalization of the Galactic component slightly lower than 1 and that of the isotropic component slightly exceeding 1. The two normalization constants also appear to be anticorrelated.

¹² We assume a positive index for the power-law model since we define it as $dN/dE \propto E^{-\alpha}$.

5. COMBINED LIKELIHOOD ANALYSIS

As previously discussed, the analysis was performed for separate RoIs and time intervals over a set of energy bins. In each energy bin we evaluated the likelihood profile for the gamma-ray flux from asteroids using `fermipy`¹³. Figure 11 shows an example of these likelihood profiles for RoI 0 in August 2008; in the figure the values of $\Delta \ln \mathcal{L} = \ln \mathcal{L}_{max} - \ln \mathcal{L}$ are shown as a function of the spectral energy distribution (SED) in the various energy bins from 56 MeV to 1.78 TeV. The likelihood values as a function of the SED are computed by varying the parameter $N_{0,\gamma}$ in Eq. 19 and keeping the spectral index fixed to the reference value of 2 in each energy bin.

All the likelihood profiles evaluated in the different RoIs, time intervals and individual energy bins have been combined to evaluate constraints on a possible source population with any given spectral shape $f(E)$, with free normalization C . Starting from the log-likelihood values $\ln \mathcal{L}_i^s$ in the i -th energy bin and s -th RoI/time bin as a function of the gamma-ray flux $Cf(E)$, it is possible to calculate the log-likelihood value $\ln \mathcal{L}_i^s(C)$ for this spectral model in each RoI/time bin. The total log-likelihood for the model is given by:

$$\ln \mathcal{L}(C) = \sum_s \sum_i \ln \mathcal{L}_i^s(C) \quad (21)$$

As a starting point, we find the value C_{max} of the normalization constant yielding the maximum likelihood. Then, we evaluate the TS of the model as $-2[\ln \mathcal{L}(C=0) - \ln \mathcal{L}(C_{max})]$, where $\ln \mathcal{L}(C=0)$ is the log-likelihood value for $C=0$, corresponding to the null hypothesis. The UL at 95% CL on the normalization factor is the value of C for which $\ln \mathcal{L}(C) = \ln \mathcal{L}(C_{max}) - 2.71/2$.

This approach is more powerful than the analysis of individual RoIs in restricted time intervals in the search of a possible tiny gamma-ray signal from a population of identical sources. Figure 12 shows the ULs at 95% CL on the power-law fluxes with spectral index 2 obtained by combining the data for individual RoIs in all time intervals and the data for all RoIs in all time intervals, compared with the limits obtained in the analyses of individual RoIs in individual time intervals. We see that the ULs obtained by combining all the time intervals in an individual RoI are a factor 10 stronger than those obtained in the analysis of the same RoI in an individual time interval. A further improvement of almost a factor

¹³ <https://fermipy.readthedocs.io/en/latest/advanced/sed.html>

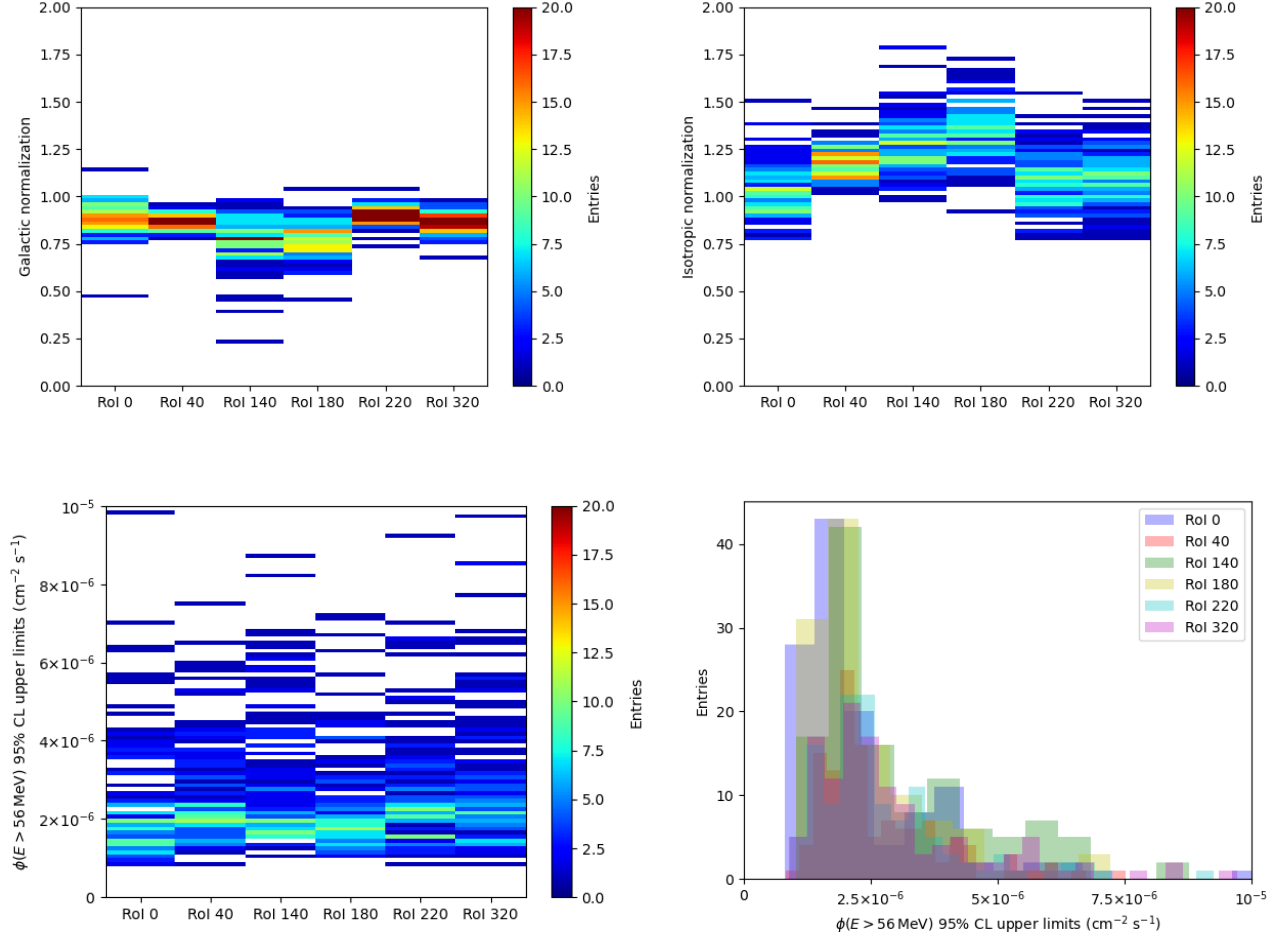


Figure 10. Summary of the fit results. Top left panel: distribution of the values of the normalization constant of the Galactic diffuse background. Top right panel: distribution of the values of the normalization constant of the isotropic background. Bottom left panel: distribution of the ULs at 95% CL on the asteroid gamma-ray flux. Bottom right panel: comparison between the distributions of the ULs at 95% CL in the six RoIs. A total of 741 fits have been performed, corresponding to about 124 fits for each RoI.

10 is obtained combining the data from all RoIs and all time intervals.

5.1. Population model-independent analysis: constraints on $N_{tot}(r)$

We have implemented the analysis procedure illustrated above using for the asteroid source the spectral intensity shape model $f(E) = I_\gamma(E, r)$ (see Eq. 15) with fixed values of the asteroid radius. This approach allows for setting constraints on $N_{tot}(r)$ for each value of the radius r . We calculated the upper limit on $N_{tot}(r)$ assuming that all asteroids have the same radius and the same composition.

We find that the signal from the asteroids is not significant and we evaluate the constraints on the normalization constant C . The UL at 95% CL on the gamma-ray flux, expressed as $\bar{C}I_\gamma(E, r)$ can be converted into an upper limit on $N_{tot}(r)$, hereafter

indicated as $N_{UL}(r)$, from Eq. 15 integrated over the whole sky:

$$\begin{aligned} \phi_{\gamma, UL}(E, r) &= \bar{C}I_\gamma(E, r) = \mathcal{B}\pi r^2 I_\gamma(E, r) N_{UL}(r) \\ \implies N_{UL}(r) &= \frac{\bar{C}}{\mathcal{B}\pi r^2} \end{aligned} \quad (22)$$

where \mathcal{B} is the integral over the entire sky of the asteroid distribution in Eq. 18 and shown in the bottom panel of Figure 8.

In Figure 13 we show the TS and the ULs at 95% CL on the total number of asteroids obtained in the hypothesis that all bodies in the population have the same radius r , assuming for $I_\gamma(E, r)$ the spectra produced by cosmic rays following either the LIS or the spectrum at Earth detected by the AMS-02 experiment interacting with silica, C-type or S-type bodies. The dependence of the TS and of the ULs on r is determined

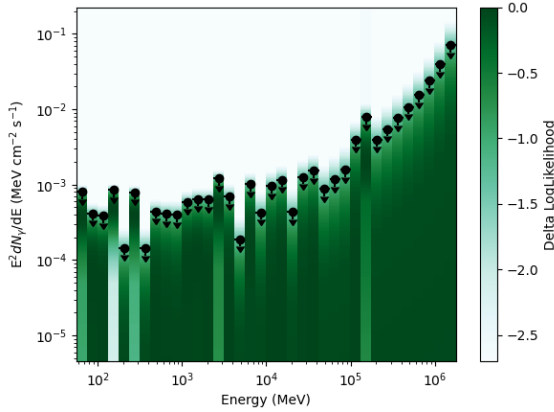


Figure 11. Spectral Energy Distribution (SED) and log-likelihood scan with respect to its maximum value for the asteroids model in RoI 0, August 2008. The color gradient shows the values of $\Delta \ln \mathcal{L}$; the black dots indicate the values of the SED where $\Delta \ln \mathcal{L} = -2.71/2$ and therefore correspond to the ULs at 95% confidence level on the SED.

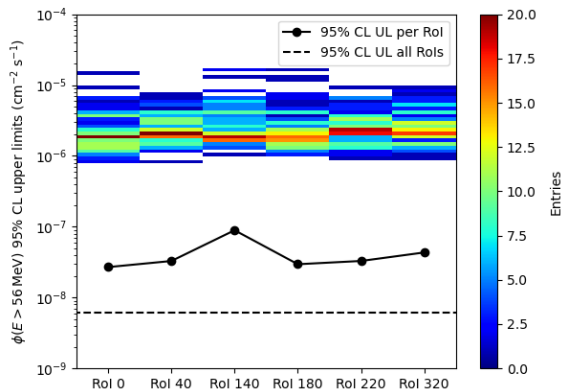


Figure 12. Summary of the ULs at 95% CL on the asteroid flux above 56 MeV. The limits obtained from the analysis of individual RoIs in individual one-month time intervals are compared with those obtained from the analysis of individual RoIs combining all time interval (filled circles, continuous line) and with those obtained from the combined analysis of all RoIs and all time intervals (dashed line).

by the shape of the function $I_\gamma(E, r)$. For $r > 10$ m, the TS is almost constant, since the gamma-ray intensity becomes independent of the asteroid radius and $N_{UL}(r)$ scales as r^{-2} . This also explains the slight increase in the ULs for $r \sim 10$ m. For smaller radii, the spectral shape of the gamma-ray intensity is harder, and it is more disfavored by the data, resulting in a TS closer to zero. The constraints obtained with the different classes of asteroids are similar for radii below 10 m and above 100 m. Since the TS does not exceed the value of

~ 10 , the asteroid source is not significantly detected for any value of r tested in the present work. In the right panel of Figure 13, we also show the number of SSSBs in the JPL catalog and the one predicted by our model (see Section 2). The distribution is calculated using a logarithmic binning in radius with 16 bins per decade. We remark that the UL obtained with this procedure cannot be directly compared with the assumed size distribution, since each upper limit is derived in the hypothesis that all bodies have the same radius r .

5.2. Model-dependent analysis: constraints on $N_{tot}(r \geq r_{min})$

We also applied the combined likelihood analysis technique to set a constraint on the asteroids population model proposed in Section 2 as an extrapolation of the model of Durda et al. (1998) for $r \leq 1.25$ km and following the JPL catalog distribution for $r \geq 1.25$ km.

The cumulative flux of asteroids can be evaluated from Eq. 15 by summing over all the radii from r_{min} up to $r_f \simeq 300$ km:

$$\phi_{\gamma,c}(E) = \mathcal{B} \sum_{r=r_{min}}^{r_f} \pi r^2 I_\gamma(E, r) N_{tot}(r). \quad (23)$$

For a given value of r_{min} , the function $f(E)$ is then given by Eq. 23. The ULs on the normalization factor C are then converted into ULs on the cumulative population model.

The left panel of Fig. 14 shows the TS of the model as a function of the minimum radius r_{min} for silica, C-type and S-type asteroids, evaluated assuming either the LIS or the spectra of cosmic rays at Earth measured by AMS-02. The TS is approximately null for $r_{min} < 10^{-3}$ km, while it increases for larger values of r_{min} , due to the change of shape of the gamma-ray intensity at the production. Compared with the results in the previous section, the increase is smoother, since, for each value of r_{min} , $f(E)$ is obtained from a folding of all the energy spectra of asteroids with $r \geq r_{min}$. At some point the TS reaches a limiting value ~ 10 , still not significant. As already stated in the previous section, this behavior is due to the fact that for large radii the spectral shape becomes independent of the asteroid size.

In the right panel of Fig. 14, the ULs at 95% CL for the integral population of asteroids with $r \geq r_{min}$ are shown. The limits are above the model in the whole range of r_{min} and the ratio between the UL and the population predicted by the model increases with r_{min} , from $\approx 10^2$ for $r_{min} = r_0 = 10$ cm to $\approx 10^6$ for $r_{min} = r_f \approx 300$ km.

5.3. Comparison between asteroids and Moon flux

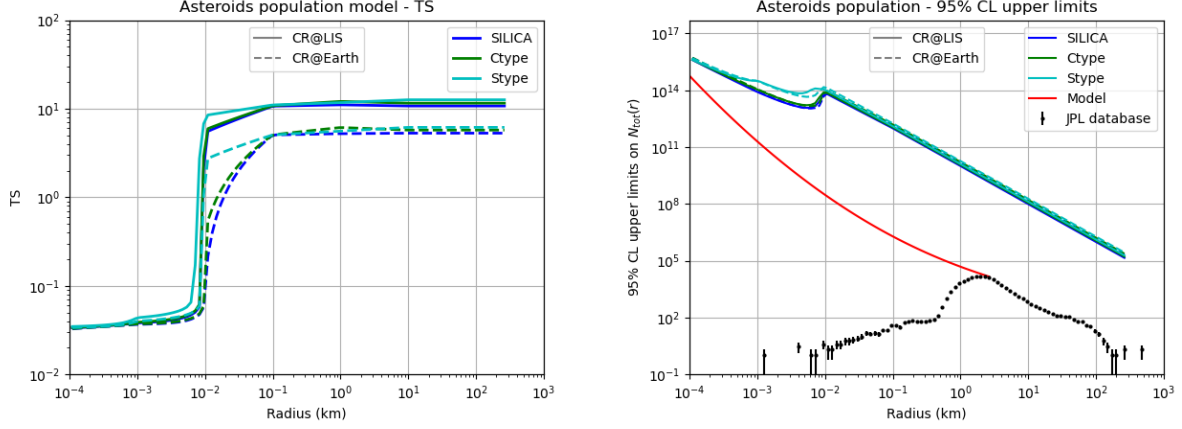


Figure 13. Left panel: TS for the asteroid component as a function of the asteroid radius obtained from the model independent analysis. The values have been calculated for silica, C-type and S-type asteroids, assuming that gamma rays are produced by cosmic rays following either the LIS (blue points) or the spectrum at Earth (green points). Right panel: ULs at 95% CL on the total number of asteroids of radius r as a function of the asteroid radius, obtained from the model-independent analysis. The red line represents our population model, which is the extrapolated Durda et al. (1998) model, while the black dots represent the data in the JPL catalog. The data and model distributions are binned in radius r with a logarithmic binning of 16 bins per decade.

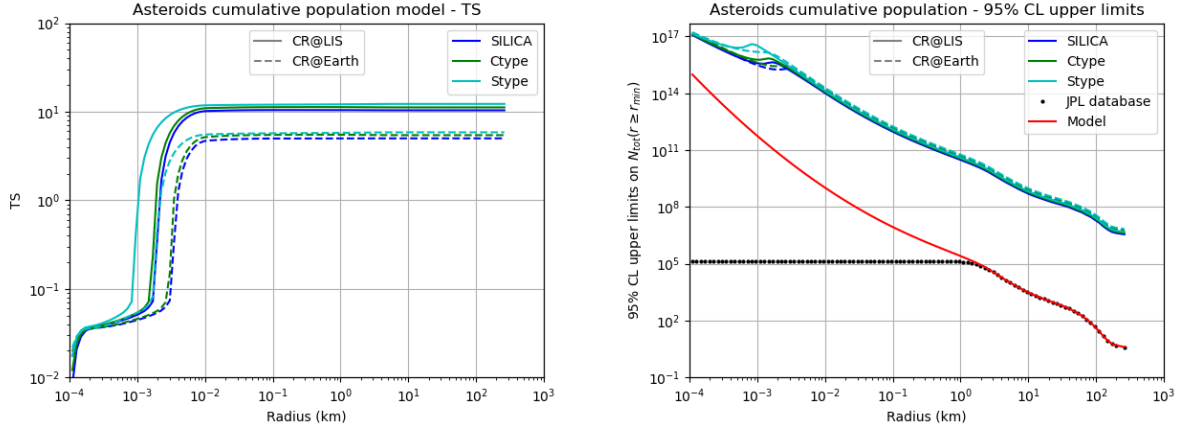


Figure 14. Left panel: TS for the asteroid component as a function of the minimum asteroid radius obtained from the model dependent analysis. The values have been calculated for silica, C-type and S-type asteroids, assuming that gamma rays are produced by cosmic rays following either the LIS (blue points) or the spectrum at Earth (green points). Right panel: ULs at 95% CL on the asteroids population as a function of the asteroid radius obtained from the model dependent analysis. The red line represents our population model, which is the extrapolated Durda et al. (1998) model, while the black dots represent the data in the JPL catalog. The data and model distributions are binned in radius r with a logarithmic binning of 16 bins per decade.

We repeated the combined likelihood analysis using for the spectral model $f(E)$ the Moon gamma-ray flux measured by the LAT in its first seven years of operation (Ackermann et al. 2016). The UL at 95% CL on the asteroid flux ϕ_A^{UL} is 0.39 times the Moon flux.

We have evaluated the ratio between the asteroid flux and the Moon flux ϕ/ϕ_{Moon} using Eq. 8 under the following assumptions: (i) the asteroids are all located at a distance $d = 2.7$ AU from the Earth; (ii) the asteroids are all composed of silica with a density of 2 g/cm^3 ; (iii)

the asteroid size distribution follows a power-law with index α , according to Eq. 1. The integration limits were fixed to the values $r_0 = 1 \times 10^{-4}$ km and $r_1 = 470$ km. Figure 15 shows the ratio ϕ/ϕ_{Moon} as a function of the power-law index α for different values of the total asteroid mass. In the left panel the gamma-ray flux from asteroids is evaluated using the CR spectra measured at Earth, while in the right panel it is evaluated using the CR LIS. The dotted line represents the value obtained from the combined analysis performed using the average

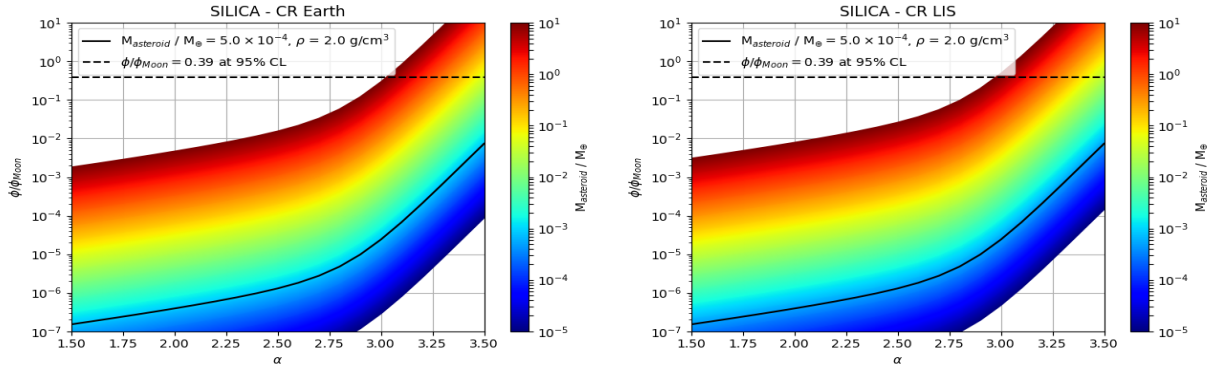


Figure 15. Ratio between the asteroid flux and the Moon flux calculated with Eq. 8, as a function of the asteroid size distribution power-law index α , for different values of the asteroid total mass. All asteroids have been assumed to lie at a distance $d = 2.7$ AU from the Earth. The gamma-ray intensity at production is obtained simulating the interaction of CRs with silica bodies. The plot in the left panel is obtained using the CR spectra measured at Earth, while the plot in the right panel is obtained using the CR LIS. The continuous black lines indicate the results obtained assuming for the total asteroid mass the value $5 \times 10^{-4} M_{\oplus}$. The dashed lines correspond to the measured UL at 95% CL.

Moon flux as spectral model. At 95% CL, all values of α and asteroid total masses above this threshold can be ruled out.

In Figure 16, the same ratio is shown as calculated in Eq. 11, i.e. assuming the gamma-ray intensity from asteroids at production to be equal to the gamma-ray intensity from the Moon at production. When using Eq. 11, the ratio ϕ/ϕ_{Moon} is independent of energy, and depends only on geometrical parameters.

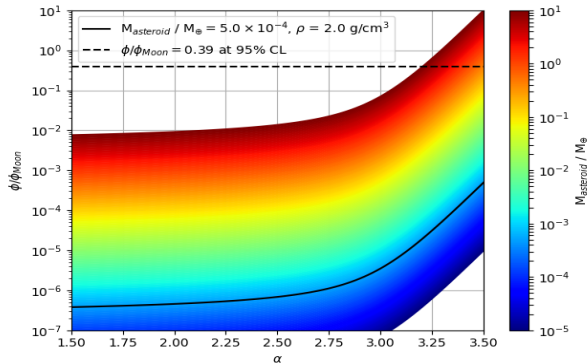


Figure 16. Ratio between the asteroids flux and the Moon flux calculated with Eq. 9 as a function of the asteroid size distribution power-law index α , for different values of the asteroid total mass.

6. CONCLUSIONS

In this work we have used the LAT Pass 8 ULTRACLEANVETO data collected from August 2008 to December 2020 to study the gamma rays from the ecliptic plane with energies in the range 56 MeV – 1 TeV, aiming to constrain the gamma-ray emission from SSSBs. Such bodies are mostly located around

the ecliptic plane and are expected to act as passive sources of gamma rays due to the interactions of cosmic rays with their surfaces. This method provides a unique way to constrain the population of all small bodies with diameters < 2 m, on which no data are available in the JPL catalog of SSSBs (Jet Propulsion Laboratory 2022).

In addition, this analysis allows for testing different models of the population of asteroids. In particular, we have used the analysis results to constrain a size distribution model (in the hypothesis that asteroids are spherical) that we have built by extrapolating the (Durda et al. 1998) model for diameters down to $\simeq 20$ cm and using the JPL catalog for diameters larger than 2.5 km.

The analysis was performed in six different RoIs at a distance $> 17^\circ$ from the Galactic plane to avoid the bright contamination of the latter. Separate analyses were performed for individual RoIs in each year and each month of the selected sample. This choice was motivated to search, in case of a source detection, for a signal modulated by solar activity over 12 years of data, and by the changes of the distance between the Earth and the asteroids as the Earth orbits the Sun.

The gamma-ray emission from each RoI was modeled including the standard diffuse background templates developed by the Fermi-LAT collaboration and the point-like and extended sources from the 4FGL catalog. An additional source describing the asteroids diffuse emission was implemented. Its morphology was built by sampling 10^7 times the asteroids orbital parameters from the JPL SSSBs catalog, while its spectral emission was modeled as a power-law of index 2. The analysis was performed with free normalizations of the most significant sources in each RoI and the prefactor N_0 of

the asteroids power-law energy spectrum. For each fit, we computed the TS of the source and we found that the asteroids source was not detected.

As a second step, we computed the SED of the asteroids in each RoI-time bin in which the data sample was divided, and we implemented a combined likelihood analysis to constrain the asteroids population. We assumed the asteroids flux to be given by the model in Eq. 15, i.e. by the convolution of the asteroids spatial map and their intensity at production level, weighted by the number $N(r)$ of asteroids with radius r and the factor πr^2 . The intensity at the production site was computed with the `Fluka` code by simulating the interactions of charged cosmic rays with bodies of different radius. As for the CR spectra, we adopted both a spectrum near the Earth, measured by the AMS-02 experiment, and the LIS spectrum, taken from De La Torre Luque et al. (2021a,b, 2022), and we assumed different asteroid composition models. We tested both homogeneous compositions and more realistic ones representing the most abundant species of asteroids. The TS of the possible asteroid source is $\lesssim 10$ for any model considered, which corresponds to a significance of approximately 3σ , insufficient for claiming a detection. We used the model of Eq. 15 to convert the ULs on the flux into ULs on $N_{tot}(r)$, assuming that all asteroids have the same radius and composition. We found that the population ULs at 95% CL vary between 4.0×10^{15} for $r \simeq 10^{-4}$ km and 1.4×10^5 for $r \simeq 300$ km with the LIS spectrum, and between 5.2×10^{15} for $r \simeq 10^{-4}$ km and 2.0×10^5 for $r \simeq 300$ km) with the Earth spectrum.

Then, we used the combined likelihood analysis to constrain the cumulative population of asteroids in our model, assuming the asteroids flux given by Eq. 23. Again, we computed the TS of this model and we found again 10.5, which is still not significant. The ULs at 95% CL on the cumulative population of asteroids are about 100 times larger than the predictions of the model for $r \simeq 10^{-4}$ km.

We remark here that the simulation code can be customized to model any asteroid composition and density. Nonetheless, the present LAT data analysis showed that the constraints on the asteroid population do not significantly change when using different asteroid composition models, mainly due to the current LAT sensitivity for this gamma-ray extended source.

Finally, we repeated the combined likelihood analysis by assuming the asteroids flux to be given by the average Moon flux measured by the LAT in its first seven years of operation. In the hypothesis that the asteroids size distribution is described by a power-law of index α , the UL of the flux provides a threshold to the values

that the asteroids mass and α can assume (see Eqs. 4, 9 and 11). This comparison is motivated by the fact that the gamma-ray emission of individual asteroids is expected to be similar to that of the Moon, once the proper differences in terms of composition, density and size are taken into account. We found an upper limit at 95% CL of 0.39 for the ratio between the asteroids and the Moon fluxes. Assuming that all asteroids are composed of silica with a density of 2 g/cm³ and are at a distance from the Earth of 2.7 AU, this constrains the asteroids mass and α to assume all values below the dashed line in Figures 15 and 16.

ACKNOWLEDGMENTS

The Fermi LAT Collaboration acknowledges generous ongoing support from a number of agencies and institutes that have supported both the development and the operation of the LAT as well as scientific data analysis. These include the National Aeronautics and Space Administration and the Department of Energy in the United States, the Commissariat à l’Energie Atomique and the Centre National de la Recherche Scientifique / Institut National de Physique Nucléaire et de Physique des Particules in France, the Agenzia Spaziale Italiana and the Istituto Nazionale di Fisica Nucleare in Italy, the Ministry of Education, Culture, Sports, Science and Technology (MEXT), High Energy Accelerator Research Organization (KEK) and Japan Aerospace Exploration Agency (JAXA) in Japan, and the K. A. Wallenberg Foundation, the Swedish Research Council and the Swedish National Space Board in Sweden.

Additional support for science analysis during the operations phase is gratefully acknowledged from the Istituto Nazionale di Astrofisica in Italy and the Centre National d’Études Spatiales in France. This work performed in part under DOE Contract DE-AC02-76SF00515.

Facility: *Fermi (Fermi-LAT)*

Software: python: <https://www.python.org/>, Van Rossum & Drake (2009); matplotlib: <https://matplotlib.org/>, Hunter (2007); ROOT: <https://root.cern/>, Brun & Rademakers (1997); HEALPix, healpy: <http://healpix.jpl.nasa.gov/>, <https://healpix.sourceforge.io/>, (Gorski et al. 2005); FLUKA: <http://www.fluka.org/fluka.php>, Ferrari et al. (2005); Böhlen et al. (2014); Battistoni et al. (2015); DPMJET: Roesler et al. (2001); PEANUT: Fassò et al. (2000); Battistoni et al. (2006) .

APPENDIX

A. YIELD AND INTENSITY AT PRODUCTION

Figure 17 and Figure 18 show the gamma-ray yields calculated with FLUKA, produced in the interactions of cosmic-ray protons, helium nuclei and electrons with silica bodies of different radii, from 10 cm to 10 km. The yields have been calculated on a grid of primary energies from 100 MeV/n up to 10 TeV/n with a spacing of 16 bins per decade and of gamma-ray energies from 0.1 MeV up to 100 MeV with a spacing of 32 bins per decade and from 100 MeV up to 10 TeV with a spacing of 8 bins per decade.

The bottom panels of the figures show the corresponding gamma-ray intensities at production sites, evaluated by folding the gamma-ray yields with the spectra of the cosmic-ray species interacting with the asteroids. The contributions to the gamma-ray intensities from individual cosmic-ray species are also shown. We have performed this calculation assuming for different CR species the energy spectra measured at Earth or the Local Interstellar Spectra (LIS). The latter have been taken from De La Torre Luque et al. (2021a,b, 2022), while for the spectra at Earth we used the AMS02 measurements (see the text for more details). We see that the average energy of gamma rays produced by each cosmic-ray species decreases as the asteroid radius increases. This feature becomes relevant for radii > 1 m; correspondingly, the gamma-ray intensities at production from each species become softer. Finally, the error bars (shown only for the total intensities) represent the statistic uncertainties due to the finite number of CR events used in the simulation to evaluate the yields.

REFERENCES

- Abdo, A. A., et al. 2009, *Astropart. Phys.*, 32, 193, doi: [10.1016/j.astropartphys.2009.08.002](https://doi.org/10.1016/j.astropartphys.2009.08.002)
- Abdollahi, S., et al. 2017, *Phys. Rev. D*, 95, 082007, doi: [10.1103/PhysRevD.95.082007](https://doi.org/10.1103/PhysRevD.95.082007)
- . 2020, *The Astrophysical Journal Supplement Series*, 247, 33, doi: [10.3847/1538-4365/ab6bcb](https://doi.org/10.3847/1538-4365/ab6bcb)
- Ackermann, M., et al. 2012, *The Astrophysical Journal Supplement Series*, 203, 4, doi: [10.1088/0067-0049/203/1/4](https://doi.org/10.1088/0067-0049/203/1/4)
- . 2016, *Phys. Rev. D*, 93, 082001, doi: [10.1103/PhysRevD.93.082001](https://doi.org/10.1103/PhysRevD.93.082001)
- Aguilar, M., et al. 2014, *Phys. Rev. Lett.*, 113, 221102, doi: [10.1103/PhysRevLett.113.221102](https://doi.org/10.1103/PhysRevLett.113.221102)
- . 2015a, *Phys. Rev. Lett.*, 114, 171103, doi: [10.1103/PhysRevLett.114.171103](https://doi.org/10.1103/PhysRevLett.114.171103)
- . 2015b, *Phys. Rev. Lett.*, 115, 211101, doi: [10.1103/PhysRevLett.115.211101](https://doi.org/10.1103/PhysRevLett.115.211101)
- . 2017, *Phys. Rev. Lett.*, 119, 251101, doi: [10.1103/PhysRevLett.119.251101](https://doi.org/10.1103/PhysRevLett.119.251101)
- Ambrosi, G., et al. 2017, *Nature*, 552, 63, doi: [10.1038/nature24475](https://doi.org/10.1038/nature24475)
- Atwood, W., Albert, A., Baldini, L., et al. 2013, arXiv e-prints, arXiv:1303.3514, <https://arxiv.org/abs/1303.3514>
- Atwood, W. B., et al. 2009, *Astrophys. J.*, 697, 1071, doi: [10.1088/0004-637X/697/2/1071](https://doi.org/10.1088/0004-637X/697/2/1071)
- Battistoni, G., Cerutti, F., Engel, R., et al. 2006, in *Proc. 11th Int. Conf. Nucl. React. Mech.* Milano: Università degli studi di Milano, 483–95
- Battistoni, G., Böhlen, T., Cerutti, F., et al. 2015, *Annals of Nuclear Energy*, 82, 10, doi: [10.1016/j.anucene.2014.11.007](https://doi.org/10.1016/j.anucene.2014.11.007)
- Böhlen, T., Cerutti, F., Chin, M., et al. 2014, *Nuclear Data Sheets*, 120, 211, doi: [10.1016/j.nds.2014.07.049](https://doi.org/10.1016/j.nds.2014.07.049)
- Brun, R., & Rademakers, F. 1997, *Nucl. Instrum. Meth. A*, 389, 81, doi: [10.1016/S0168-9002\(97\)00048-X](https://doi.org/10.1016/S0168-9002(97)00048-X)
- Davis, D. R., Durda, D. D., Marzari, F., Campo Bagatin, A., & Gil-Hutton, R. 2002, *Asteroids III*, 545
- De Gaetano, S., Mazziotta, M. N., Loparco, F., & Giglietto, N. 2021, *PoS, ICRC2021*, 607, doi: [10.22323/1.395.0607](https://doi.org/10.22323/1.395.0607)
- De La Torre Luque, P., Mazziotta, M. N., Ferrari, A., et al. 2022, *JCAP*, 07, 008, doi: [10.1088/1475-7516/2022/07/008](https://doi.org/10.1088/1475-7516/2022/07/008)
- De La Torre Luque, P., Mazziotta, M. N., Loparco, F., Gargano, F., & Serini, D. 2021a, *JCAP*, 03, 099, doi: [10.1088/1475-7516/2021/03/099](https://doi.org/10.1088/1475-7516/2021/03/099)
- . 2021b, *JCAP*, 07, 010, doi: [10.1088/1475-7516/2021/07/010](https://doi.org/10.1088/1475-7516/2021/07/010)
- Dohnanyi, J. S. 1969, *Journal of Geophysical Research* (1896-1977), 74, 2531, doi: [10.1029/JB074i010p02531](https://doi.org/10.1029/JB074i010p02531)
- Duffett-Smith, P., & Zwart, J. 2011, *Practical Astronomy with your Calculator or Spreadsheet* (Cambridge University Press)

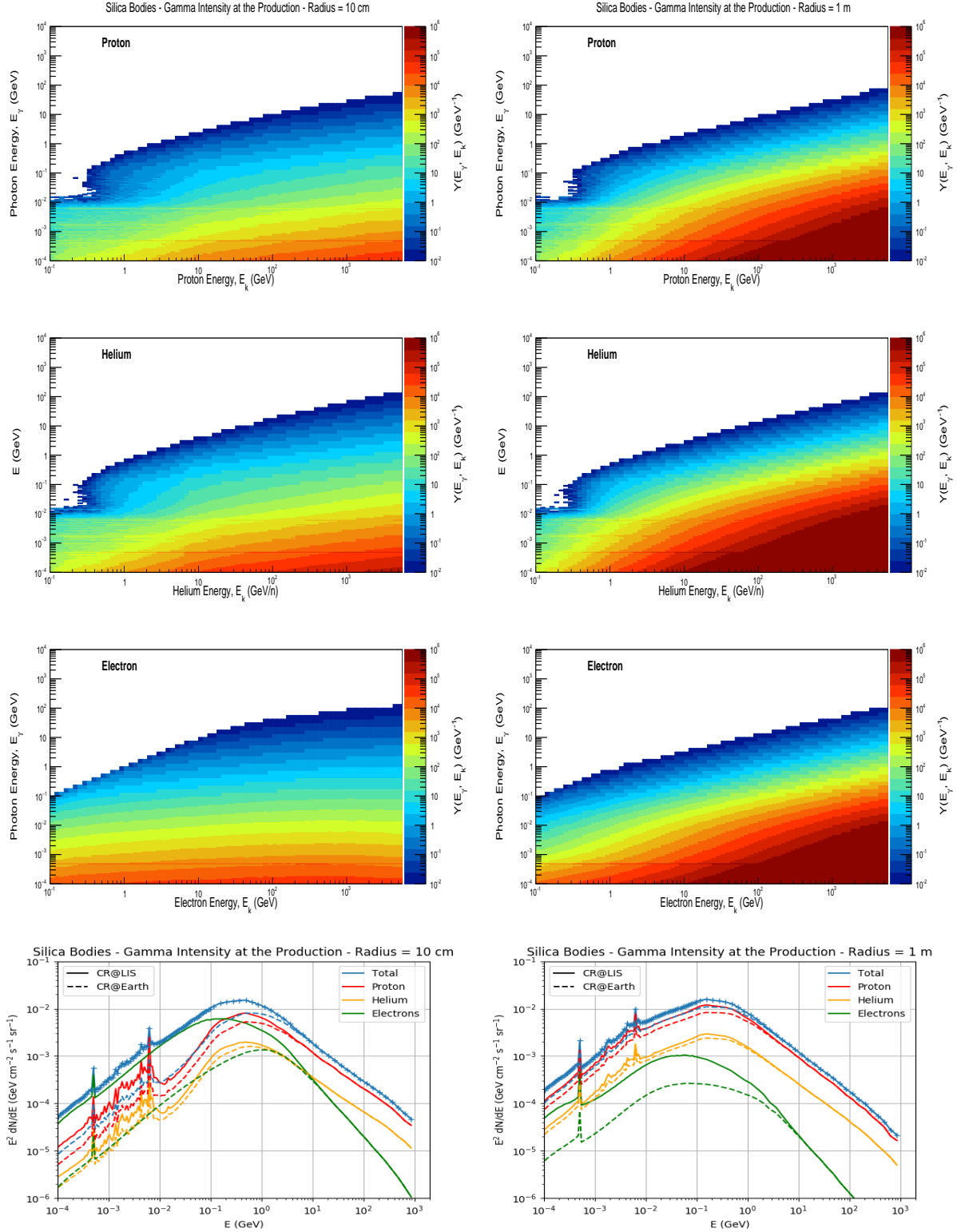


Figure 17. Yields of gamma rays produced by the interactions of protons, ^4He and electrons with a silica body. The bottom plots show the gamma-ray intensities at the production obtained using the CR LIS spectra (continuous lines) and the CR spectra measured at Earth (dashed lines). Left column: body radius of 10 cm; right column: body radius of 1 m.

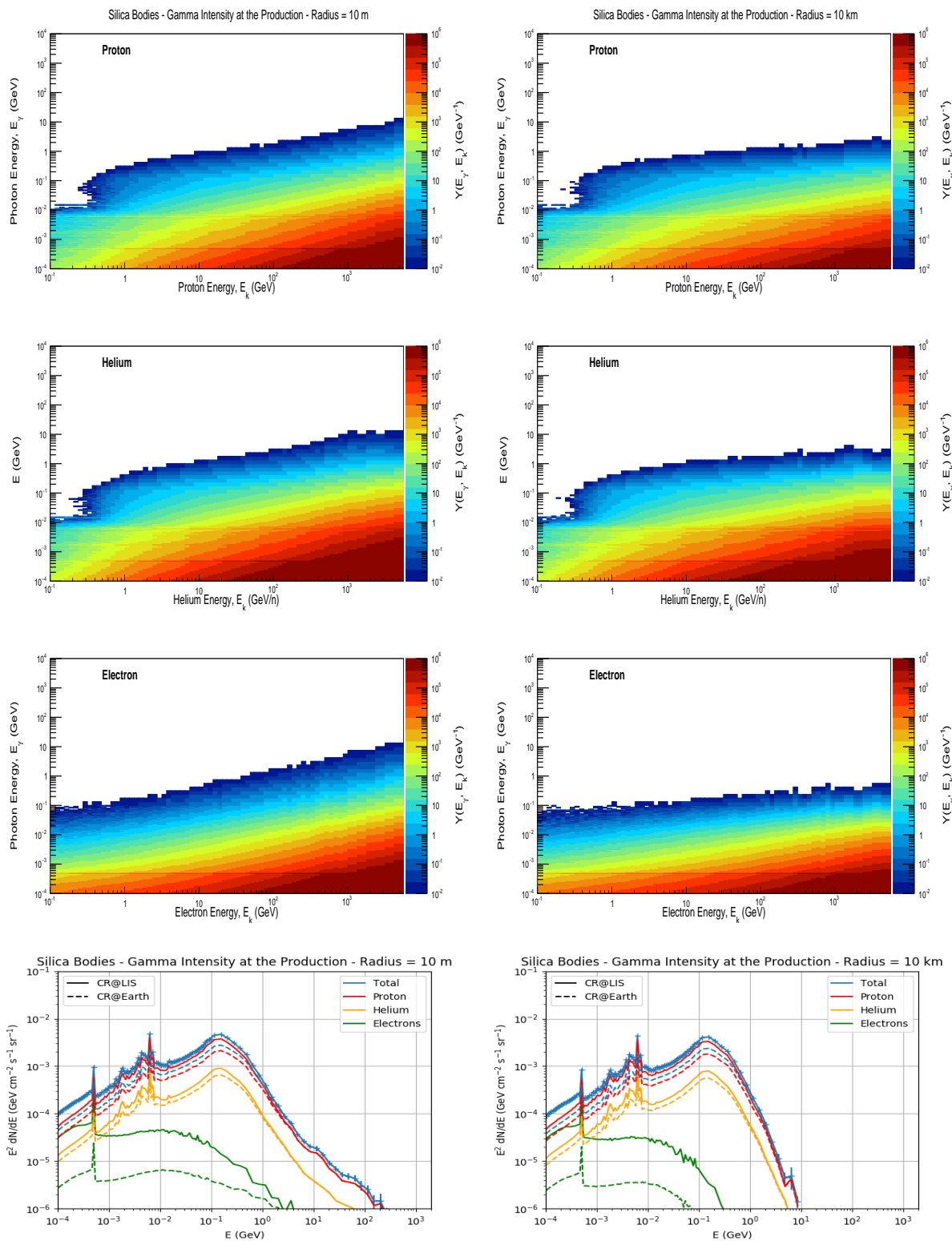


Figure 18. Yields of gamma rays produced by the interactions of protons, ^4He and electrons with a silica body. The bottom plots show the gamma-ray intensities at the production obtained using the CR LIS spectra (continuous lines) and the CR spectra measured at Earth (dashed lines). Left column: body radius of 10 m; right column: body radius of 10 km.

- Durda, D., Greenberg, R., & Jedicke, R. 1998, *Icarus*, 135, 431, doi: [10.1006/icar.1998.5960](https://doi.org/10.1006/icar.1998.5960)
- Fassò, A., Ferrari, A., Sala, P. R., & Ranft, J. 2000, in *Advanced Monte Carlo for radiation physics, particle transport simulation and applications. Proceedings, Conference, MC2000, Lisbon, Portugal, October 23-26, 2000*, 955–960
- Ferrari, A., Sala, P. R., Fassò, A., & Ranft, J. 2005, doi: [10.2172/877507](https://doi.org/10.2172/877507)
- Gorski, K. M., Hivon, E., Banday, A. J., et al. 2005, *Astrophys. J.*, 622, 759, doi: [10.1086/427976](https://doi.org/10.1086/427976)
- Hunter, J. D. 2007, *Computing in Science & Engineering*, 9, 90, doi: [10.1109/MCSE.2007.55](https://doi.org/10.1109/MCSE.2007.55)
- Jedicke, R., & Metcalfe, T. 1998, *Icarus*, 131, 245, doi: [10.1006/icar.1997.5876](https://doi.org/10.1006/icar.1997.5876)
- Jet Propulsion Laboratory. 2022, *Small-Body Database*, <https://ssd.jpl.nasa.gov/tools/sbdb.lookup.html#/>
- Lodders, K., & Fegley, B. 1998, *The planetary scientist's companion* / Katharina Lodders, Bruce Fegley.
- Mazziotta, M. N., Cerutti, F., Ferrari, A., et al. 2016, *Astropart. Phys.*, 81, 21, doi: [10.1016/j.astropartphys.2016.04.005](https://doi.org/10.1016/j.astropartphys.2016.04.005)
- Mazziotta, M. N., De La Torre Luque, P., Di Venere, L., et al. 2020, *Phys. Rev. D*, 101, 083011, doi: [10.1103/PhysRevD.101.083011](https://doi.org/10.1103/PhysRevD.101.083011)
- Moskalenko, I. V., & Porter, T. A. 2009, *Astrophys. J.*, 692, 54, doi: [10.1088/0004-637X/692/1/L54](https://doi.org/10.1088/0004-637X/692/1/L54)
- Moskalenko, I. V., Porter, T. A., Digel, S. W., et al. 2008, *Astrophys. J.*, 681, 1708, doi: [10.1086/588425](https://doi.org/10.1086/588425)
- Pitjeva, E., & Pitjev, N. 2018, *Astronomy Letters*, 44, 554
- Roesler, S., Engel, R., & Ranft, J. 2001, in *Advanced Monte Carlo for Radiation Physics, Particle Transport Simulation and Applications*, ed. A. Kling, F. J. C. Barão, M. Nakagawa, L. Távora, & P. Vaz (Berlin, Heidelberg: Springer Berlin Heidelberg), 1033–1038
- Van Rossum, G., & Drake, F. L. 2009, *Python 3 Reference Manual* (Scotts Valley, CA: CreateSpace)
- Wikipedia. 2022, *Orbital elements* — Wikipedia, The Free Encyclopedia, https://en.wikipedia.org/wiki/Orbital_elements
- Wood, M., Caputo, R., Charles, E., et al. 2018, *PoS, ICRC2017*, 824, doi: [10.22323/1.301.0824](https://doi.org/10.22323/1.301.0824)